China Ocean Eng., 2021, Vol. 35, No. 3, P. 317–331
DOI: https://doi.org/10.1007/s13344-021-0030-3, ISSN 0890-5487
http://www.chinaoceanengin.cn/ E-mail: coe@nhri.cn

Numerical Simulation of Solitary Wave Forces on A Vertical Cylinder on A Slope Beach

KUAI Yan-rong[a], ZHOU Ji-fu[a, b, *], DUAN Jin-long[a], WANG Xu[a]

[a] Key Laboratory for Mechanics in Fluid Solid Coupling Systems, Institute of Mechanics, Chinese Academy of Sciences, Beijing 100190, China

[b] School of Engineering Sciences, University of Chinese Academy of Sciences, Beijing 100049, China

Received November 10, 2020; revised February 23, 2021; accepted March 22, 2021

Abstract

Wave forces acting on a vertical cylinder at different locations on a slope beach in the near-shore region are investigated considering solitary waves as incoming waves. Based on the Reynolds-averaged Navier−Stokes equations and the k–ε turbulence model, wave forces due to the interaction between the solitary wave and cylinder are simulated and analyzed with different incident wave heights and cylinder locations. The numerical results are first compared with previous theoretical and experimental results to validate the model accuracy. Then, the wave forces and characteristics around the cylinder are studied, including the velocity field, wave surface elevation and pressure. The effects of relative wave height, Keulegan−Carpenter (KC) number and cylinder locations on the wave forces are also discussed. The results show that the wave forces exerted on a cylinder exponentially increase with the increasing incident wave height and KC number. Before the wave force peaks, the growth rate of the wave force shows an increasing trend as the cylinder moves onshore. The cylinder location has a notable effect on the wave force on the cylinder in the near-shore region. As the cylinder moves onshore, the wave force on the cylinder initially increases and then decreases. For the cases considered here, the maximum wave force appears when the cylinder is located one cylinder diameter below the still-water shoreline. Furthermore, the fluid velocity peaks when the maximum wave force appears at the same location.

Key words: wave force, cylinder location, Reynolds-averaged Navier–Stokes equations, solitary wave, numerical simulation

Citation: Kuai, Y. R., Zhou, J. F., Duan, J. L., Wang, X., 2021. Numerical simulation of solitary wave forces on a vertical cylinder on a slope beach. China Ocean Eng., 35(3): 317–331, doi: https://doi.org/10.1007/s13344-021-0030-3

1 Introduction

Vertical cylinders are widely used as an important component of coastal structures, such as sea-crossing bridges and offshore wind turbine foundations. These structures inevitably undergo wave forces owing to complicated environmental conditions, especially for vertical cylinders. Because the wave forces acting on a cylinder have significant engineering relevance to the safety of such coastal structures, it is important to investigate the wave forces exerted on cylinders to ensure structural safety. For practical reasons, many cylinders are constructed in the near-shore region (FEMA, 2004) where wave breaking frequently occurs. The resulting flow patterns and hydrodynamic loading of breaking waves on cylinders differ significantly from those for non-breaking waves (Alagan Chella et al., 2015; Xiao and Huang, 2015), which makes it more difficult to accurately estimate the wave forces on cylinders in the near-shore region.

The interaction between waves and cylinders has received considerable attention over the past several decades. There have been a few widely accepted results for wave forces on structures located on a flat bed (Zhao et al., 2007; Yang et al., 2015; Bonakdar et al., 2015; Kamath et al., 2015; Aristodemo et al., 2017; Tripepi et al., 2018). For instance, the Morison formula is often used to estimate the wave force acting on a single small-scale pile (Morison et al., 1950), which accounts for the inertial and drag components of wave forces using empirical coefficients. However, when a wave propagates into the near-shore region, it becomes asymmetric and the wave front steepness increases, which results in wave breaking (Hsiao et al., 2008; Chang et al., 2009; Hsieh et al., 2016; Kuai et al., 2018a). The Moris-

Foundation item: This study was financially supported by the National Key R&D Program of China (Grant No. 2017YFC1404202), the National Natural Science Foundation of China (Grant No. 11572332) and the Strategic Priority Research Program of the Chinese Academy of Sciences (Grant Nos. XDB22040203 and XDA22000000).

*Corresponding author. E-mail: zhoujf@imech.ac.cn

on formula can thus not be directly applied in this case to estimate the wave forces because the breaking waves are associated with extreme impact forces over a short duration (Bredmose and Jacobsen, 2010; Choi et.al., 2015). To calculate such impact forces, an impact force term is considered in the Morison equation in addition to quasi-static forces to describe the total force owing to breaking waves (Goda et al., 1966). However, several involved parameters, such as the slamming coefficients, curling factor and breaker shape, are not easily determined.

Wave forces on structures in the near-shore region have been investigated by several numerical studies. For instance, Mo et al. (2013) studied a plunging solitary wave and its interaction with a slender cylinder on a slope beach using filtered Navier–Stokes equations with large eddy simulation turbulence modeling. Correspondingly, the surface elevation, velocity and wave profile during wave−cylinder interaction were well illustrated. Choi et al. (2015) investigated the breaking wave impact forces on vertical and inclined cylinders based on the modified Navier–Stokes equations to study the dynamic amplification factor owing to the structural response. Kuai et al. (2018b) studied wave forces acting on complex bridge substructures in the near-shore region based on the Reynolds-averaged Navier–Stokes (RANS) equations and k–ε turbulence model. However, the water depth at the structure location was large and the wave deformation was unclear and non-breaking.

Some studies have shown that cylinder location plays an important role in its interaction with waves in the near-shore region (Wienke and Oumeraci, 2005; Alagan Chella et al., 2017). For instance, Xiao and Huang (2015) examined wave forces on a cylinder in the near-shore region located at seven different locations, including locations above and below the still-water shoreline on a slope beach. However, they mainly focused on snapshots of wave−cylinder interaction and the time history of wave forces on the cylinder. Kamath et al. (2016) investigated the effects of breaker location on the wave force of a vertical cylinder on a slope bottom. The location of the cylinder was changed according to the wave breaking stage, including a smaller range of cylinder locations. Alagan Chella et al. (2017) explored the effect of relative distance between the breaking point and cylinder on the breaking wave forces, and mainly focused on the relationship between the characteristics and geometric properties of breaking solitary waves and the resulting impact forces on structures. Although the aforementioned studies reported many useful results regarding wave forces on cylinders at different locations, few studies have addressed the change rule of the velocity field and pressure around a cylinder when the cylinder moves onshore.

High loads on offshore structures caused by extreme events (e.g., tsunamis) also are of great significance in engineering design. Tsunamis are very long waves generated by earthquakes or landslides that can produce highly destructive damage to coastal structures (Mori et al., 2011). Because tsunami characteristics depend on the seabed deformation conditions, it is difficult to develop a universally applicable tsunami wave model (Aristodemo et al., 2020). For simplicity, solitary waves are usually used as an incident wave to study tsunami characteristics (Adityawan et al., 2013; Sælevik et al., 2013), sediment transport (Alsina et al., 2009; Sumer et al., 2011), and coastal structures (Alagan Chella et al., 2017; Kuai et al., 2018b; Zhao et al., 2019; Aristodemo et al., 2020).

In this study, numerical investigations were carried out on wave forces acting on a cylinder at different locations in the near-shore region owing to solitary waves. The interaction between the solitary waves and cylinders was simulated based on the unsteady RANS equations coupled with a k–ε turbulence model. The variation of the wave force with different incident wave heights and KC numbers were correspondingly studied and the effects of cylinder locations on the wave forces, velocity fields, pressure and wave surface elevation were analyzed.

2 Numerical model

2.1 Governing equations and numerical schemes

2.1.1 *Governing equations*

The unsteady RANS equations are incorporated into standard k–ε turbulence model. The model is then applied to simulate wave−cylinder interaction on a uniform slope beach. The governing equations for an incompressible fluid are expressed as follows:

Continuity equation:

$$\frac{\partial u_i}{\partial x_i} = 0. \tag{1}$$

Momentum equation:

$$\frac{\partial u_i}{\partial t} + u_j \frac{\partial u_i}{\partial x_j} = -\frac{1}{\rho}\frac{\partial p}{\partial x_i} + g_i + \frac{\partial}{\partial x_j}\left(\upsilon \frac{\partial u_i}{\partial x_j} - \overline{u_i' u_j'}\right), \tag{2}$$

where i and j are the cyclic coordinates in an orthogonal coordinate system whose values are 1, 2 and 3; x_i is the spatial coordinates; t is the time coordinate; u_i is the time-averaged velocity components; p is the pressure; ρ is the fluid density; g_i is the gravitational acceleration; υ is the kinematic viscosity; $-\overline{u_i' u_j'}$ denotes the turbulent Reynolds stresses, which can be expressed as $-\overline{u_i' u_j'} = \nu_t(\partial u_i/\partial x_j + \partial u_j/\partial x_i) - 2k\delta_{ij}/3$, where ν_t is the turbulence eddy viscosity. In this study, ν_t is simulated using the standard k–ε turbulence model proposed by Launder and Spalding (1974), which are as follows:

$$\frac{\partial k}{\partial t} + u_j \frac{\partial k}{\partial x_j} = \frac{\partial}{\partial x_j}\left[\left(\frac{\upsilon_t}{\sigma_k} + \upsilon\right)\frac{\partial k}{\partial x_j}\right] + G - \varepsilon; \tag{3}$$

$$\frac{\partial \varepsilon}{\partial t} + u_j \frac{\partial \varepsilon}{\partial x_j} = \frac{\partial}{\partial x_j}\left[\left(\frac{\upsilon_t}{\sigma_\varepsilon} + \upsilon\right)\frac{\partial \varepsilon}{\partial x_j}\right] + C_{1\varepsilon}\frac{\varepsilon}{k}G - C_{2\varepsilon}\frac{\varepsilon^2}{k}, \tag{4}$$

where k is the turbulent kinetic energy; ε is the turbulent kinetic dissipation rate; G is the turbulent production term, and five related coefficients suggested by the original author are used: $C_\mu = 0.09$, $C_{1\varepsilon} = 1.44$, $C_{2\varepsilon} = 1.92$, $\sigma_k = 1.0$, $\sigma_\varepsilon = 1.3$.

2.1.2 *Numerical schemes*

Eqs. (1) and (2) are numerically solved by a two-step projection method with finite volume spatial discretization (Issa, 1986). The linear least square reconstruction method is adopted to evaluate the gradients at the cell centers (Barth, 1992). The time derivative is discretized by the forward time difference method. The first and second-order accuracy is obtained for the temporal and spatial terms, respectively.

The volume of fluid (VOF) method is used to trace or capture the free surface (Hirt and Nichols, 1981). The governing equation is as follows:

$$\frac{\partial F}{\partial t} + \frac{\partial u_i F}{\partial x_i} = 0, \tag{5}$$

where F is the volume fraction, which is defined as:

$$F(x,t) = \begin{cases} 0 & \text{air} \\ 0 < F < 1 & \text{interface} \\ 1 & \text{water} \end{cases} \tag{6}$$

The piecewise-linear interface calculation method is used to solve the VOF governing equation (Youngs, 1982). It assumes that the interface between the air and water has a linear slope within each cell and uses this linear shape to calculate fluid advection through the cell faces.

2.2 Computational setting and initial and boundary conditions

2.2.1 *Computational setting*

The computational domain for calculating the wave force acting on a cylinder in the near-shore region is shown in Fig. 1, in which the seabed is simplified to a uniform slope and the coordinate origin is located at the toe of the beach slope. The computational domain is 440 m long, 20 m wide and 22.8 m high. The wave-maker is located on the left side and the solitary wave travels in the x-direction. The simulations are carried out by using a computer with 8 cores and 16 threads, and the computation for each case lasts about 2−3 days.

In Fig. 1, β represents the angle between the slope beach and x-coordinate, x and y are the horizontal coordinates, and z is the vertical coordinate. The wave model is applied to simulate wave−cylinder interaction with the cylinder located at eleven different locations on the slope beach, labeled as ①–⑪ in Fig. 1. For comparison, Cylinder ① is located on the flat bed where the flow field is not affected by the slope beach. Cylinder ⑩ is located at the still-water shoreline and Cylinder ⑪ is located 10 m above the still-water shoreline. Cylinders ②–⑨ are located on the slope beach between the toe of the slope and still-water shoreline.

2.2.2 *Initial and boundary conditions*

In the computational domain, the piston-type wave-maker is located on the left and the nonlinear algorithms developed by Goring (1978) are used to generate solitary waves. The motion of piston-type wave-maker is governed by equations as follows (Katell and Eric, 2002):

$$X(t) = S_G \tanh\left[7.6\left(t/t^* - 0.5\right)\right]; \tag{7}$$

$$t^* = \frac{4}{\beta c}\left[\tanh^{-1}(0.999) + \frac{H}{h}\right]; \tag{8}$$

$$S_G = 4\sqrt{Hh/3},\ \beta = \sqrt{\frac{3H}{h^3}},\ c = \sqrt{g(H+h)}, \tag{9}$$

where $X(t)$ is the displacement of the piston-type wave-maker varying with time; H is the solitary wave height; h is the still water depth; t is the time; c is the wave celerity.

The wave propagates from left to right. The boundaries of the computational domain include the pressure-inlet boundary on the top, a solid no-slip wall at the bottom and on the slope. Both the front and back of the computational domain are set to symmetric boundaries. At the initial time, the water velocities in the entire computational zone are set to zero.

2.3 Mesh description and model validation

2.3.1 *Mesh description*

Both the structured and unstructured grids are used in the simulation, as shown in Fig. 2. Finer meshes are used in

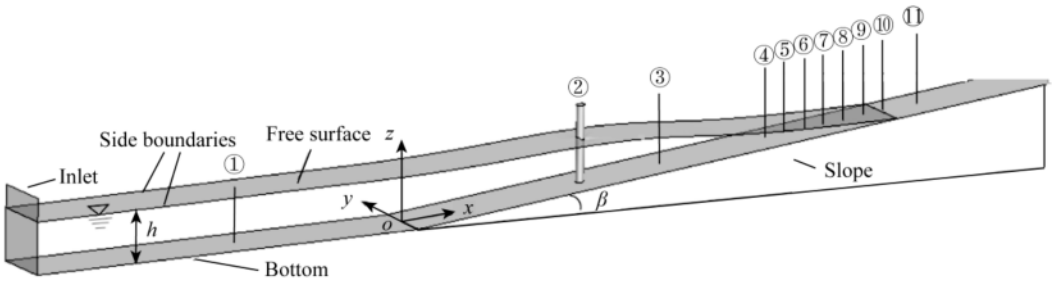

Fig. 1. Sketch of the calculation model.

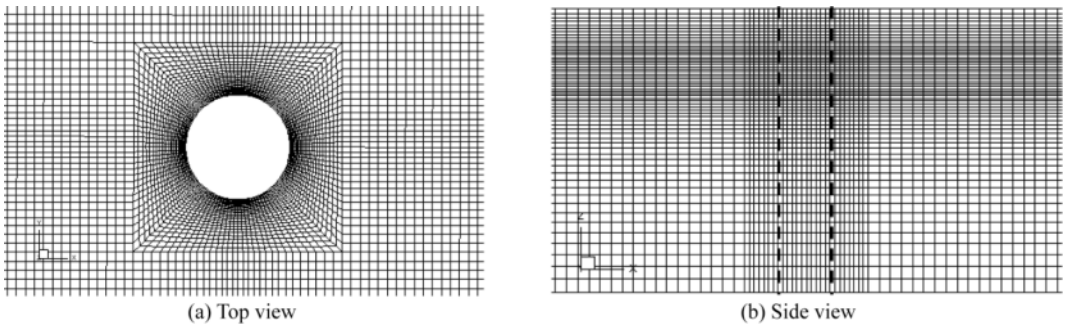

Fig. 2. Diagram of the mesh.

areas near the water surface and cylinder. The influence of grid size on the computational results is firstly investigated. Four different grid sizes were examined, which are defined as M1, M2, M3 and M4, shown in Table 1. The computed time histories of wave surface elevations and wave forces with these four grid sizes as well as experimental data (H/h=0.40, Yates and Wang, 1994) are shown in Fig. 3 and Fig. 4, respectively. The results show that the numerical results with the coarser grid (M3 and M4) are much smaller than the results of the experiment. However, the numerical results of M1 and M2 show a good agreement with the experimental results. But it should be noted that no significant improvement can be achieved for wave surface elevations and wave forces when the grid is refined from M2 to M1. To balance the calculation precision and speed, the mesh size of $\Delta x_{\min} = \dfrac{L}{115}$ ($\Delta y_{\min} = \dfrac{L}{115}$) and $\Delta z_{\min} = \dfrac{H}{16}$ (Grid M2) is adopted.

Based on the comparison of numerical results and experimental data, this method of mesh grid choice has been proved accurate. Therefore, the same method is used to determine the grid sizes for all the cases in this paper. The grids are non-uniform in the horizontal direction with sizes varying from $\Delta x_{\min}$ (or $\Delta y_{\min}$) = 0.3 m to $\Delta x_{\max}$ (or $\Delta y_{\max}$) = 0.8 m, and in the vertical direction with sizes varying from $\Delta z_{\min} = H/18$ to $\Delta z_{\max}$ = 1.2 m, where H is the solitary wave height. The selected mesh size represents a compromised

Table 1 Detail of mesh sizes

Mesh label	M1	M2	M3	M4
Number	2805600	1907698	1231758	874620
$\Delta x_{\min}$ (m)	L/153	L/115	L/92	L/77
$\Delta y_{\min}$ (m)	L/153	L/115	L/92	L/77
$\Delta z_{\min}$ (m)	H/20	H/16	H/13	H/10

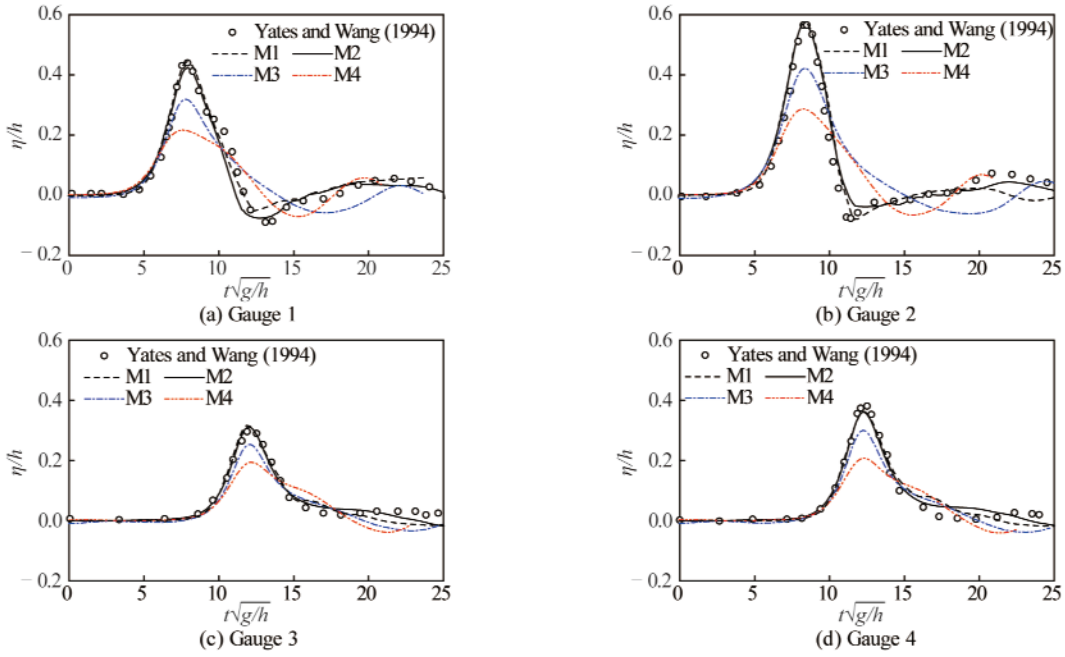

Fig. 3. Comparison of time histories of wave surface elevations (H/h = 0.40).

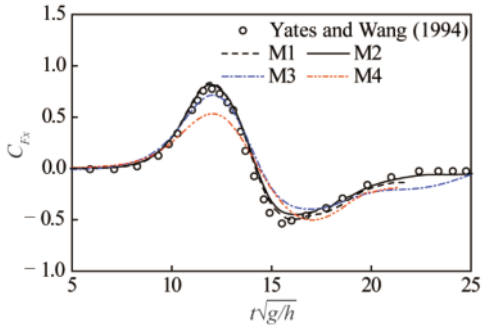

Fig. 4. Comparison of time histories of wave forces (H/h = 0.40).

choice in accordance with the calculation accuracy and computational resources. The optimization of the time step, Δt, is subject to the Courant number constraint $Cr = \sqrt{gh}\Delta t/\Delta x < 1$.

2.3.2 *Model validation*

The model is validated to examine the accuracy of the wave generation and wave force exerted on the cylinder based on the theoretical solution of a solitary wave and experiments conducted by Yates and Wang (1994). To validate the accuracy of solitary wave generation, a reference gauge is used to monitor the wave surface elevation (Synolakis, 1987), where the flow is considered as the potential flow, and nonlinear effects and viscosity have little effect on wave propagation. A comparison of the solitary wave surface elevation calculated by the simulation and the first-order theory of Boussinesq et al. (1872) (Eq. (10)) is shown in Fig. 5, in which the wave surface elevation η is normalized by the still-water depth h and the time t is normalized by $\sqrt{h/g}$. This indicates that the computed solitary wave surface is slightly smaller than the theoretical result owing to energy dissipation. Overall, the validation demonstrates that the solitary waves can be well numerically generated using our simulation.

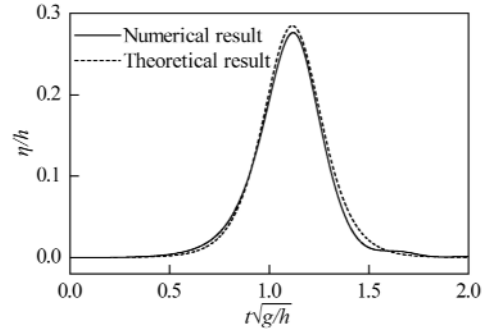

Fig. 5. Comparison of incident wave profile between numerical and theoretical results.

$$\eta = H\mathrm{sech}^2[K(x-ct)], \tag{10}$$

where $K = \sqrt{\dfrac{3H}{4h^3}}$.

By following Madsen et al. (2008), values for the effective wavelength and effective period can be defined by

$$L = \frac{2\pi}{K},\ T = \frac{2\pi}{Kc}. \tag{11}$$

The free surface elevation and wave forces on the cylinder are examined and validated by comparing the present numerical results with the experimental data of Yates and Wang (1994), who studied solitary wave scattering by a vertical cylinder. The cylinder radius R and water depth h are 0.0635 m and 0.04 m, respectively. The relative incident solitary wave height H/h is 0.018−0.40. Four wave gauges are set to monitor the time histories of the wave surfaces, which are located at 1.66R (gauge 1) and 1.03R (gauge 2) from the front of the cylinder and 1.03R (gauge 3) and 1.35R (gauge 4) from the rear of the cylinder.

The wave force acting on a cylinder is obtained by the integral of pressure and viscous stress, which is expressed as follows:

$$\boldsymbol{F} = \int_S (-p+\tau_v)\,\mathrm{d}S = \sum_{i=1}^{n}(-p+\tau_v)A\boldsymbol{n}, \tag{12}$$

where τ_v is the viscous stress, which corresponds to $v\partial u_i/\partial x_j$ in Eq. (2); S is the wetted cylinder surface; dS is the surface integral element; n is the number of surface elements; A is the element area, and $\boldsymbol{n}$ is the unit of the normal vector pointing out of the surface element. The dimensionless horizontal wave force C_{Fx} is defined as:

$$C_{Fx} = \frac{F_x}{\frac{1}{2}\rho g h^2 D}, \tag{13}$$

where F_x is the horizontal wave force acting on the cylinder; h is the still-water depth at the flat bed, and D is the cylinder diameter.

The comparisons of the wave surface elevations and wave forces between the calculated and experimental results of Yates and Wang (1994) are presented in Figs. 6 and 7. Fig. 6 shows that the time histories of the wave surface elevations for four different locations under conditions of H/h = 0.40 agree well with the experimental results. The time histories of wave forces C_{Fx} obtained by calculation and experiment are also compared in Fig. 7. The calculations and experimental results are in notably good agreement. Therefore, it can be concluded that the model used here can accurately reproduce wave forces acting on a cylinder.

3 Simulations and analysis of wave forces

3.1 Computational conditions

We mainly focus on wave−cylinder interaction on a slope beach and the solitary wave is used as an initially incoming wave. In consideration of the influence of various factors, a total of 35 cases are simulated, as listed in Table 2. Herein the applied solitary waves have a ratio of wave height to water depth H/h ranging from 0.109 to 0.424. The

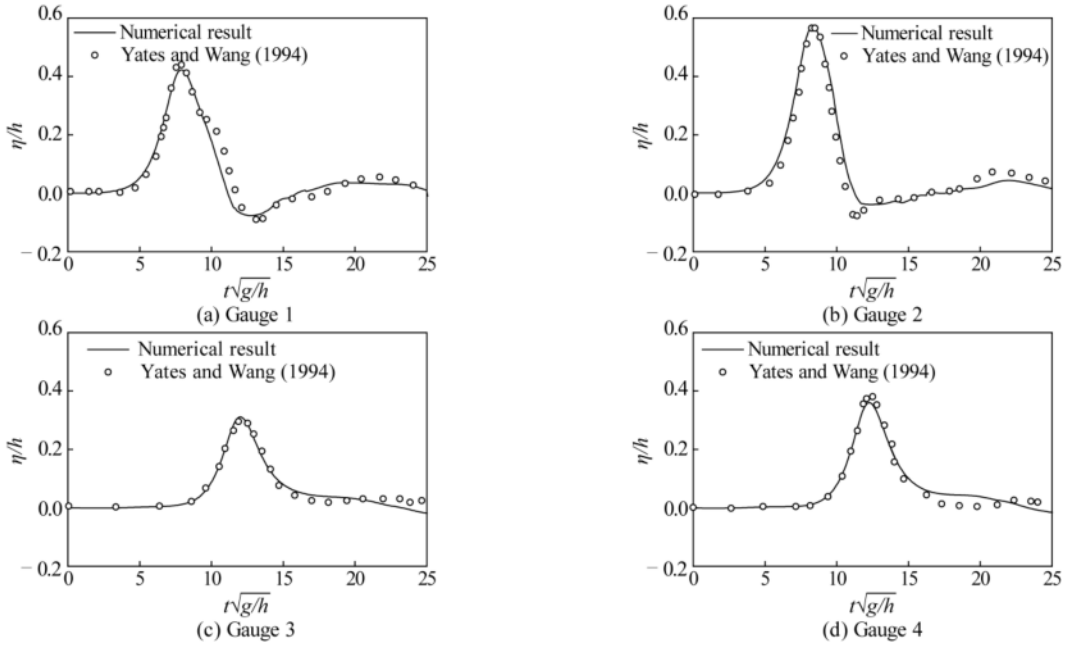

Fig. 6. Comparison of time histories of wave surface elevations (H/h = 0.40).

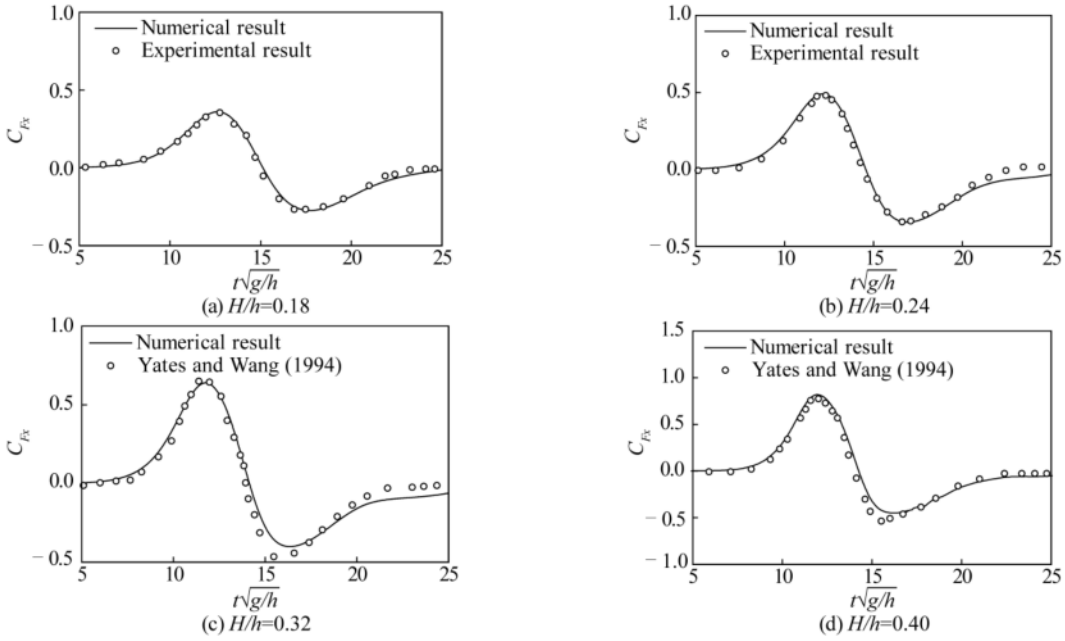

Fig. 7. Comparison of time histories of wave forces for different wave heights.

seabed in the near-shore is simplified as a uniform slope and the angle of beach slope is $\gamma = \tan\beta = 1/10$. The diameter of the cylinder D is 2.5 m and the cylinder location is expressed as x/h, varying from −4.43 to 10.63. The location with $x/h = -4.43$ is where the cylinder is located at the flat bed and not affected by the beach slope, which corresponds to Cylinder ① in Fig. 1. The location with x/h =10 is where the cylinder is located at the still-water shoreline, which corresponds to Cylinder ⑩ in Fig. 1. The location with x/h = 10.63 is where the cylinder is located above the still-water shoreline, which corresponds to Cylinder ⑪ in Fig. 1. The location with x/h = 3.37−9.92 is where the cylinder is located on the slope beach between the slope toe and still-water shoreline, which corresponds to Cylinders ②–⑨ in Fig. 1.

According to Grilli et al. (1997), the type of wave breaking, based on values of a non-dimensional slope parameter S_0, depends on the relative wave height and beach slope, which is shown in Eq. (14) as follows:

$$S_0 = 1.521\frac{\gamma}{\sqrt{H/h}}. \tag{14}$$

When $S_0 < 0.025$, the breaking type is spilling. When $0.025 < S_0 < 0.3$, the breaking type is plunging. When $0.3 <$

Table 2 Calculation conditions and parameters settings.

Cases	D (m)	h (m)	x/h	γ	H/h	H/L	S_0	KC
					0.109	0.005	0.461	15.124
					0.191	0.011	0.348	20.030
1−5	2.5	15.8	−4.43	0	0.274	0.018	0.291	24.004
					0.320	0.022	0.269	25.943
					0.424	0.032	0.234	29.846
					0.109	0.005	0.461	15.124
					0.191	0.011	0.348	20.030
6−10	2.5	15.8	3.67	1/10	0.274	0.018	0.291	24.004
					0.320	0.022	0.269	25.943
					0.424	0.032	0.234	29.846
					0.109	0.005	0.461	15.124
					0.191	0.011	0.348	20.030
11−15	2.5	15.8	5.57	1/10	0.274	0.018	0.291	24.004
					0.320	0.022	0.269	25.943
					0.424	0.032	0.234	29.846
					0.109	0.005	0.461	15.124
					0.191	0.011	0.348	20.030
16−20	2.5	15.8	8.10	1/10	0.274	0.018	0.291	24.004
					0.320	0.022	0.269	25.943
					0.424	0.032	0.234	29.846
21	2.5	15.8	8.73	1/10	0.274	0.018	0.290	24.004
22	2.5	15.8	9.37	1/10	0.274	0.018	0.290	24.004
23	2.5	15.8	9.68	1/10	0.274	0.018	0.290	24.004
24	2.5	15.8	9.84	1/10	0.274	0.018	0.290	24.004
25	2.5	15.8	9.92	1/10	0.274	0.018	0.290	24.004
					0.109	0.005	0.461	15.124
					0.191	0.011	0.348	20.030
26−30	2.5	15.8	10	1/10	0.274	0.018	0.291	24.004
					0.320	0.022	0.269	25.943
					0.424	0.032	0.234	29.846
					0.109	0.005	0.461	15.124
					0.191	0.011	0.348	20.030
31−35	2.5	15.8	10.63	1/10	0.274	0.018	0.291	24.004
					0.320	0.022	0.269	25.943
					0.424	0.032	0.234	29.846

$S_0 < 0.37$, the breaking type is surging. Thus, the breaking type is plunging for H/h = 0.274−0.424, surging for H/h = 0.191, and no wave breaks for H/h = 0.109.

The KC number is the ratio between the excursion length of the fluid particles to the width of the cylinder in the flow, which ranges from 15 to 30. The computational formula is given as follows:

$$KC = \frac{U_{\mathrm{m}}T}{D}; \tag{15}$$

$$U_{\mathrm{m}} = H\sqrt{\frac{g}{h}}, \tag{16}$$

where U_{m} is the maximum horizontal velocity of the water particle (Rayleigh, 1876).

3.2 Wave transformation and evolution

The time histories of wave surface elevations at different locations under the conditions of H/h = 0.274 are shown in Fig. 8. The locations where the time histories of wave surface elevations are monitored are from the flat bed to the positions above the still-water shoreline. The locations with x/h = −4.43, 0, and 10 are where the cylinders are placed on the flat bed, at the slope toe, and the still-water shoreline, respectively. Fig. 8 shows that the incident wave is not affected while propagating in the constant water depth region (Figs. 8a−8b). As the wave shoals on the slope, the steepening of the wave front face becomes increasingly clear and the wave gradually transforms into an approximately triangular shape (Figs. 8c−8f). During this process, the wave surface elevation gradually increases and reaches the maximum at x/h = 8.71 with a value of η/h = 0.29. The solitary wave then breaks and the wave height significantly decreases (Figs. 8g−8j).

Fig. 9 demonstrates the transformation and evolution of a solitary wave in the process of propagation over a beach slope with a relative wave height H/h of 0.274. This illustrates that the wave crest remains stable while traveling across the constant water depth region until reaching the

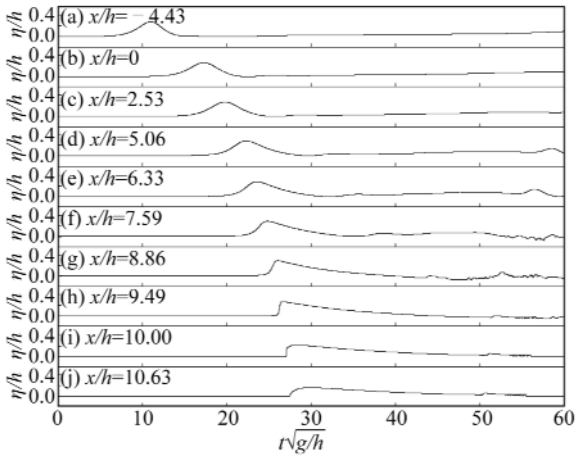

Fig. 8. Time histories of wave surface elevations for a relative incident wave height of H/h = 0.274.

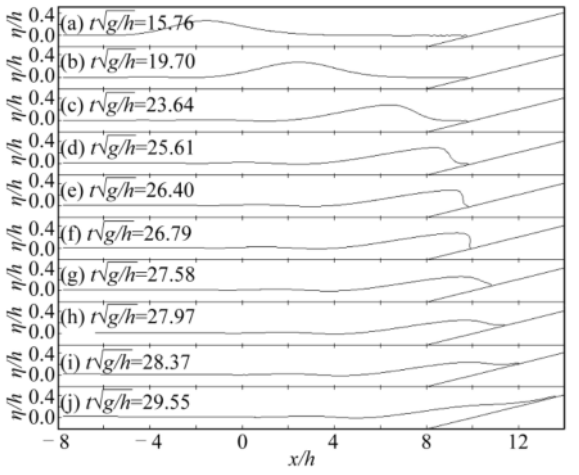

Fig. 9. Spatial wave surface elevations for the relative incident wave height H/h = 0.274.

slope toe (i.e., x/h = 0 at $t\sqrt{g/h}$ = 15.76 shown in Fig. 9a). Afterwards, the solitary wave shoals over the slope and front face of the wave crest becomes steeper until the wave eventually breaks (Figs. 9b−9f). The breaking wave then continuously runs up along the slope (Figs. 9g−9j).

The above analysis indicates that wave breaking point is located at x/h = 8.71 for H/h = 0.274. Cylinders ②–④ (i.e., x/h = 3.67−5.57) are located at the area where the wave is non-breaking, and Cylinders ⑤–⑨ (i.e., x/h = 8.73−9.92) are located in the coastal zone where the solitary wave breaks. The wave characteristics vary significantly before and after breaking, which leads to large differences of the wave forces exerted on the cylinders in different locations.

3.3 Time histories of wave forces

To investigate the influence of cylinder location on the wave force, we analyzed the time histories of wave forces for H/h=0.274 at six different locations: from the flat bed to the still-water shoreline, as shown in Fig. 10. When the cylinder is located on a flat bed or beach slope where the local

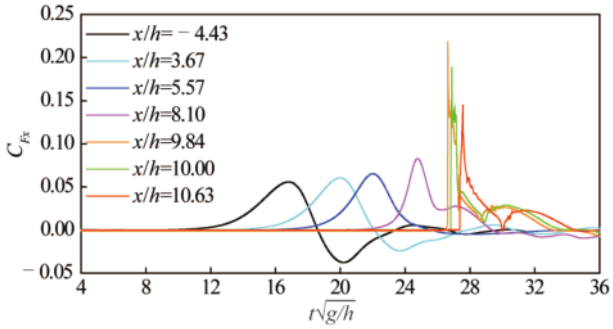

Fig. 10. Time histories of wave forces on cylinders (H/h=0.274).

still-water depth is deeper (x/h = −4.43 and x/h = 3.67), the wave force exerted on the cylinder initially increases. After the wave force reaches its positive maximal value, it decreases with wave propagation. Then a negative maximum wave force appears when the wave crest passes by the cylinder. As the cylinder locations are moved to x/h = 5.57 and 8.10, the positive maximum values are larger compared with those with x/h = −4.43 and x/h = 3.67 while the negative maximum almost disappears. Furthermore, for x/h = −4.43 to 8.10, a longer time is required for the wave force to increase from zero to the maximum value because the solitary wave is non-breaking. When the cylinder is located near the still-water shoreline, the initial water depth around the cylinder is zero or very small (x/h = 9.84, 10.00, 10.63). The time history of the wave force shows that there are two peaks of the wave forces exerted on the cylinder. The wave force increases from zero to the maximum value over a short duration, which strongly impacts the cylinder. Thus, the time histories of the wave forces are considerably more complex than that on a cylinder at constant depth (Mo et al., 2007), which is worthy of attention.

3.4 Maximum wave force

The relative wave height H/h is a parameter that describes the characteristics of a solitary wave, and the KC number is an important parameter that denotes the interaction between the wave and cylinder. For the same H/h, the maximum wave force on the cylinder for the same location x/h is defined as $C_{Fx\text{-max}}$, whereas the largest wave force on the cylinder for all locations x/h is defined here as $(C_{Fx\text{-max}})_{\max}$.

Fig. 11 shows the variations of $C_{Fx\text{-max}}$ with different relative wave heights and KC numbers. It can be seen that both the relative wave height and KC number exert an evident influence on $C_{Fx\text{-max}}$. As shown in Fig. 11a, the maximum wave force $C_{Fx\text{-max}}$ acting on the cylinder at the same location increases with relative wave height according to the rule of power exponent, which can be expressed by Eq. (17). The growth rate of the maximum wave force $C_{Fx\text{-max}}$ with relative wave height increases with x/h when the cylinders are located at x/h = −4.43 to 10.00. The growth rate of the wave force then decreases at x/h=10.63. Fig. 11b shows

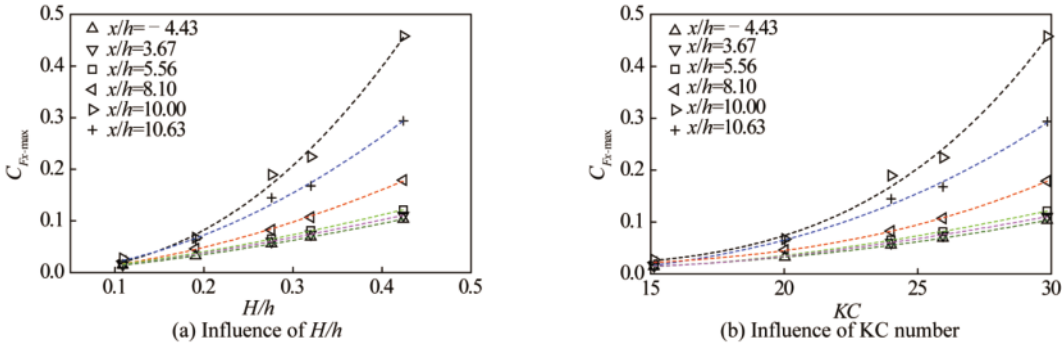

Fig. 11. Influence of the relative wave height H/h and KC number on wave forces.

the variation of wave force with KC number, which illustrates a similar changing trend as those in Fig. 11a. And the changing trend can be represented by Eq. (18).

$$C_{Fx\text{-max}} = a\left(\frac{H}{h}\right)^b, \quad R^2_{\min} = 0.9885; \tag{17}$$

$$C_{Fx\text{-max}} = c(KC)^d, \quad R^2_{\min} = 0.9880, \tag{18}$$

where a, b, c, and d are coefficients which are related to solitary wave conditions and cylinder locations; $R^2_{\min}$ is the minimum correlation coefficient.

Since the maximum wave forces $C_{Fx\text{-max}}$ acting on the cylinders vary largely with cylinder location, the maximum wave forces $C_{Fx\text{-max}}$ on the cylinder changing with cylinder locations under conditions of H/h=0.109−0.424 are shown in Fig. 12a. It can be seen that when the cylinder is located on the flat bed, the maximum wave force $C_{Fx\text{-max}}$ is the smallest for the same H/h. With increasing x/h, $C_{Fx\text{-max}}$ initially increases and then decreases with the maximum value $(C_{Fx\text{-max}})_{\max}$ appearing when the cylinder is located near the still-water shoreline.

Previous research has shown that the hydrodynamic loading on structures in shallow waters is mostly governed by the loading caused by plunging breaking waves (Alagan Chella et al., 2012). Therefore, one type of the plunging breaking wave, H/h = 0.274 is chosen for many cases during our simulation to clarify the relative location of the cylinder and still-water shoreline when $(C_{Fx\text{-max}})_{\max}$ appears, as shown in Fig. 12b. The results show that $C_{Fx\text{-max}}$ reaches the maximum of 0.22 when the cylinder is located at about x/h = 9.84, i.e., one-cylinder diameter distance below the still-water shoreline. It is different from the result that the wave force is the largest when the cylinder is located at 0.63D below the still-water shoreline in Xiao and Huang (2015), which can be attributed to the difference of the beach slope. Moreover, the value of $C_{Fx\text{-max}}$ increases by approximately three times compared with that on the flat bed. Compared with the breaking point x/h = 8.71, the maximum wave force occurs when the cylinder is located between the breaking point and still-water shoreline and is closer to the still-water shoreline. The mechanism for this process is analyzed in Section 4, including analysis of the velocity field, wave surface elevation, and pressure distribution.

4 Discussion

The wave force on a cylinder is obtained by the integral of pressure and viscous stress, as shown in Eq. (12). The analysis shows that more than 95% of the total wave force is resulted from pressure. The fluid velocity, wave surface elevation, and pressure around the cylinder are therefore analyzed herein.

4.1 Wave characteristics around the cylinder varying with time

4.1.1 *Velocity fields and wave surface elevations varying with time*

The velocity fields and wave surface elevations around

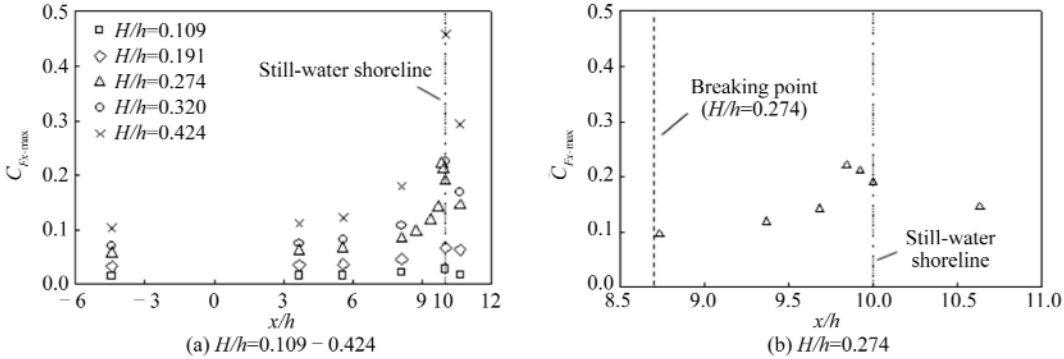

Fig. 12. Wave forces on cylinders at different locations x/h.

the cylinder at different times in the process of wave propagation under conditions of $x/h = -4.43$ and 9.84 for $H/h = 0.274$ are illustrated in Figs. 13 and 14, respectively, in which the velocity is normalized by $\sqrt{gh}$ and the time is normalized by $\sqrt{h/g}$.

Figs. 13a−13d correspond to the moments when the wave force $C_{Fx} = 0.56C_{Fx\text{-max}}$, $C_{Fx\text{-max}}$, 0 and $C_{Fx\text{-min}}$. It can be observed that the solitary wave is non-breaking when the cylinder is located at $x/h = -4.43$ and the largest fluid velocity appears at the wave crest. As shown in Fig. 13a, the wave crest is far from the cylinder and the wave surface elevation around the cylinder is small. As the solitary wave propagates, the wave crest gradually approaches the cylinder. Thus, the wave force on the cylinder increases and the maximum occurs at $t\sqrt{g/h} = 16.78$ before the wave crest reaches the cylinder (Fig. 13b). The wave force then decreases, and the wave crest passes by the cylinder (Fig. 13c). At $t\sqrt{g/h} = 20.17$, the wave surface elevation in the front of the cylinder is smaller than that in the rear of the cylinder (Fig. 13d), which leads to a negative maximum value in the time history of wave force for $x/h = -4.43$ (Fig. 10).

As shown in Fig. 14, the cylinder is located at $x/h = 9.84$, which is close to the still-water shoreline. Figs. 14a−14e demonstrate the velocity fields and wave surface elevations when the wave force $C_{Fx} = 0$, $C_{Fx} = C_{Fx\text{-max}}$, $0.60C_{Fx\text{-max}}$, $0.40C_{Fx\text{-max}}$, $0.16C_{Fx\text{-max}}$ and $0.12C_{Fx\text{-max}}$. At $t\sqrt{g/h} = 26.40$, the solitary wave breaks before the wave arrives in the front of the cylinder and the largest fluid velocities appears in the wave front at this moment (Fig. 14a). Then, the wave front touches the cylinder and the velocity on the side of the cylinder peaks (Fig. 14b). At this moment, the wave surface elevation in the front of the cylinder increases compared with that shown in Fig. 14a. And the

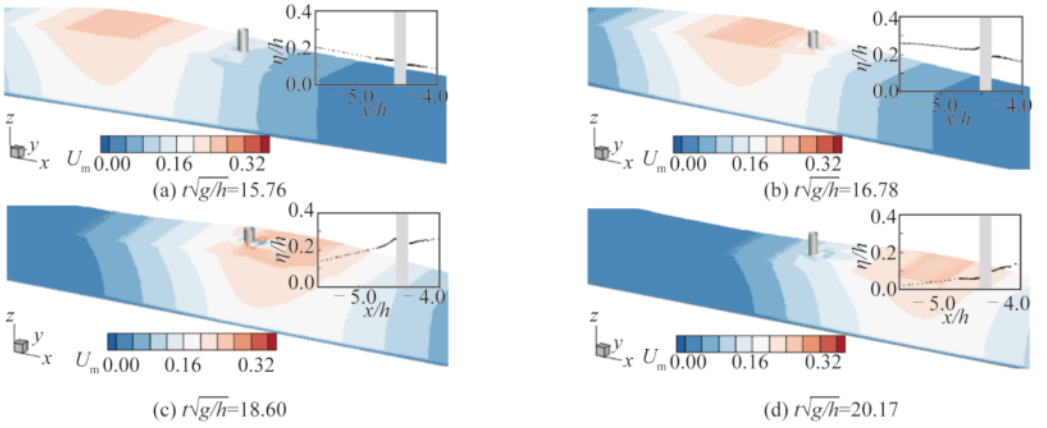

Fig. 13. Velocity fields and wave surface elevations at different times ($x/h = -4.43$, $H/h = 0.274$).

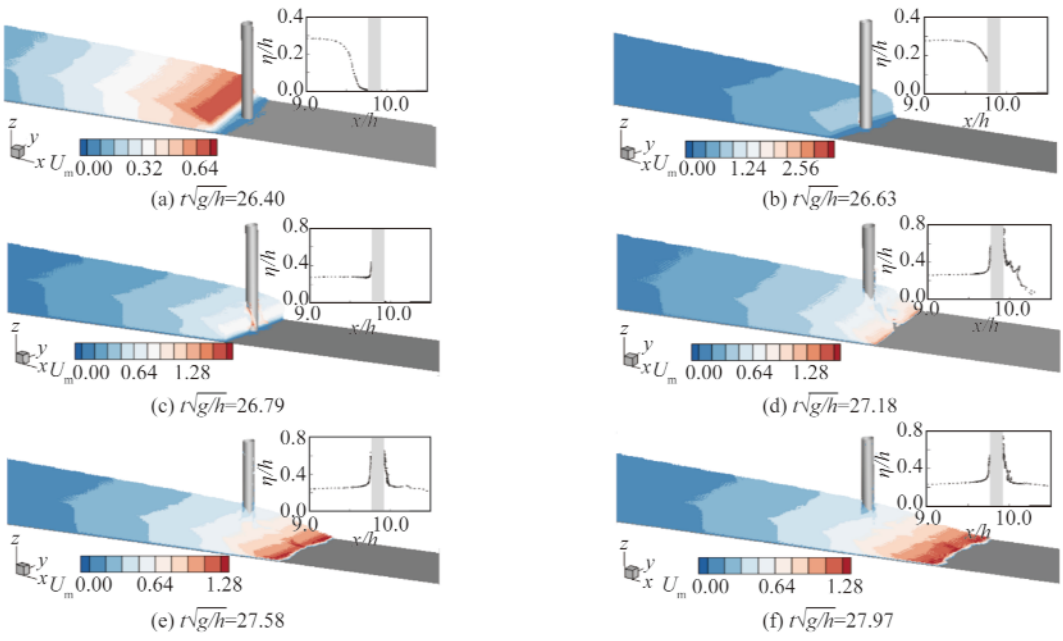

Fig. 14. Velocity fields and wave surface elevations at different times ($x/h = 9.84$, $H/h = 0.274$).

wave force on the cylinder increases and the maximum appears at $t\sqrt{g/h}$ = 26.63 before the wave surface elevation in the front of the cylinder reaches the maximum. As the water wraps around the rear of the cylinder, the maximum fluid velocity in the wave front decreases and the wave surface elevation in the front of the cylinder increases (Fig. 14c). At $t\sqrt{g/h}$=27.18 (Fig. 14d), the separated wave fronts complete their merging in the rear of the cylinder and then move forward on the beach (Fig. 14e). The maximum fluid velocity in the wave front decreases and the maximum wave surface elevation in the front of the cylinder increases during this process. Afterwards, as the solitary wave runs up on the slope beach, the kinetic energy is converted into potential energy with energy dissipation, which leads to reduced fluid velocities and reduced the maximum wave surface elevation in the front of the cylinder (Fig. 14f).

The maximum wave surface elevation of the solitary wave in the front of the cylinder, R_u, is defined as the height from the still-water level to the highest position where the wave arrives in the front of the cylinder, which is normalized by the still-water depth h. The maximum value variations of the wave forces, wave surface elevation, and fluid velocity with time are demonstrated in Fig. 15, thus, the relationship among these parameters can be investigated.

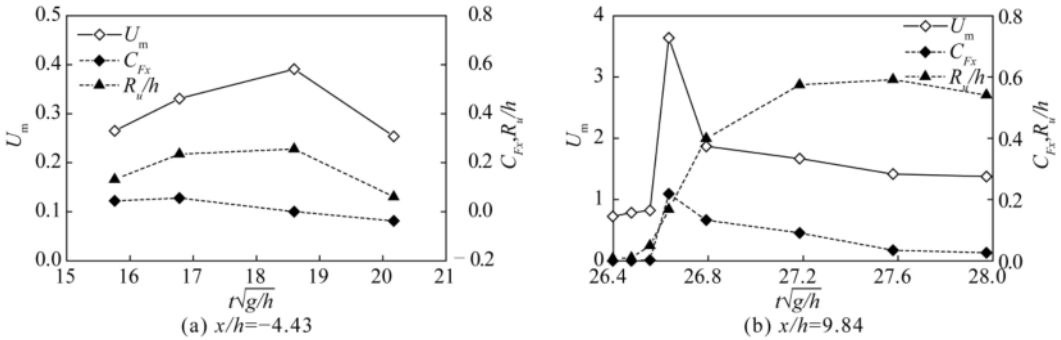

Fig. 15. Maximum fluid velocity, wave surface elevation in the front of the cylinder, and wave force being a function of time (H/h = 0.274).

The fluid velocity initially increases and then decreases, with the maximum at $t\sqrt{g/h}$=18.60 for x/h = −4.43 (Fig. 15a) and $t\sqrt{g/h}$=26.63 for x/h = 9.84 (Fig. 15b). In Fig. 15a, the maximum wave surface elevation in the front of the cylinder shows a similar changing trend with fluid velocity, and the maximum value is also observed at $t\sqrt{g/h}$=18.60 when the maximum fluid velocity appears. In addition, both the maximum fluid velocity and wave surface elevation appear after the wave force reaches its maximum value. However, Fig. 15b shows that the wave force exerted on the cylinder exhibits a similar changing trend as fluid velocity, and the maximum wave force is observed at $t\sqrt{g/h}$=26.63 when the maximum fluid velocity appears. Furthermore, both the maximum fluid velocity and wave force appear before the wave surface elevation reaches its highest point. The fluid velocity therefore plays a more significant role in wave forces on cylinders for breaking solitary waves.

4.1.2 *Pressure around the cylinder varying with time*

To further analyze the variation of wave force on the cylinder, the distribution of pressure around the cylinder at the still-water level is investigated, and the relative pressure C_P is defined as:

$$C_P = \frac{P_\eta - P_0}{\rho g h}, \tag{19}$$

where P_η is the pressure above the still-water level when the wave force C_{Fx} arrives at the maximum and P_0 is the static pressure above the still-water level at the initial state.

To further clarify the pressure around the cylinder, the circumference angle is defined as from −180° to +180° (Fig. 16). The wave incident direction in the front of the cylinder is defined as 0° and the rear of the cylinder is defined as −180° (+180°). The circumference angles for the cylinder facing the wave is from −90° to 90°, and the angle for the rear of the cylinder in this case is from −180° to –90° and from 90° to 180°.

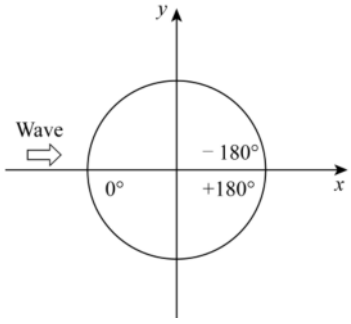

Fig. 16. Diagram of circumference angle.

The distribution of relative pressure around the cylinder above the still-water level (i.e., z = 0) at different times for the conditions of x/h = −4.43 and 9.84 is shown in Fig 17. When $t\sqrt{g/h}$=15.76 – 18.60, the largest relative pressure is located in the front of the cylinder (α = 0° and 360°) and begins to decrease from the front of the cylinder towards

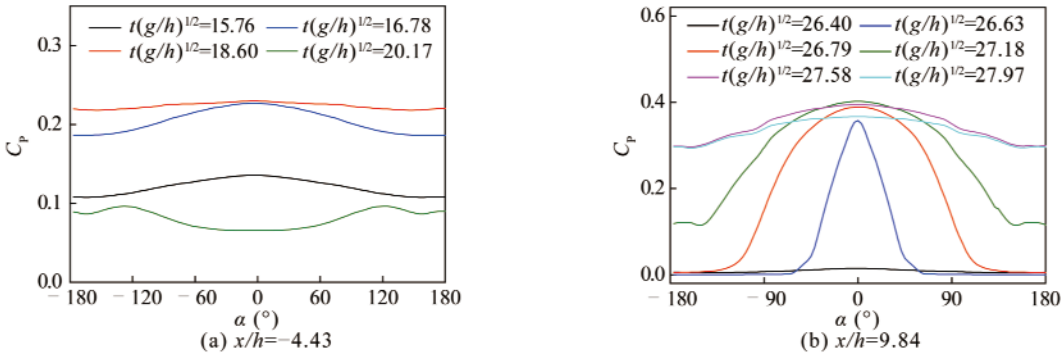

Fig. 17. Distribution of relative pressure around the cylinder varying with time (H/h = 0.274).

both sides. The largest pressure difference appears at $t\sqrt{g/h}$=16.78 when the maximum wave force is observed. At $t\sqrt{g/h}$=20.17, the wave crest has passed by the cylinder, which leads to higher pressure at the rear of the cylinder. As a result, there exists a negative maximal value in the time history of wave force for x/h = −4.43, as shown in Fig. 10.

Fig. 17b shows that the largest relative pressure is located in the front of the cylinder (α = 0°) and lower relative pressure is detected in the rear of the cylinder (α =−180° and +180°) for x/h = 9.84. At $t\sqrt{g/h}$=26.63 – 26.79, the solitary wave has not wrapped in the rear of the cylinder and a higher pressure difference is observed between α = 0° and +180°, which leads to a larger wave force. As time progresses, the wave wraps at the rear of the cylinder. The pressure at the rear of the cylinder increases significantly, leading to the decrease of pressure difference between α = 0° and +180°, such as $t\sqrt{g/h}$=27.18 – 27.58. Therefore, the wave force exerted on the cylinder decreases largely during this process. At $t\sqrt{g/h}$=27.97, the reduction of pressure in the front of the cylinder is resulted from the decreasing wave surface elevation, which leads to decreasing wave force on the cylinder.

4.2 Wave characteristics around the cylinder at different locations

4.2.1 *Velocity fields and wave surface elevations around the cylinders at different locations*

Fig. 18 shows the velocity fields and wave surface elevations around the cylinders at different locations for a solitary wave of H/h = 0.274 when the wave forces acting on cylinders reach the maximum $C_{Fx\text{-max}}$. It is indicated in Figs. 18a–18c that the solitary wave does not break before arriving at the front of the cylinder. Larger fluid velocity is observed at the wave crest. Correspondingly, the maximum wave force occurs before the solitary wave crest reaches the front of the cylinder. Moreover, the maximum wave surface elevation in the front of the cylinder is relatively small. As the cylinder moves onshore, breaking occurs for the solitary wave before it arrives in the front of the cylinder, and larger fluid velocity can be detected at the wave front, as

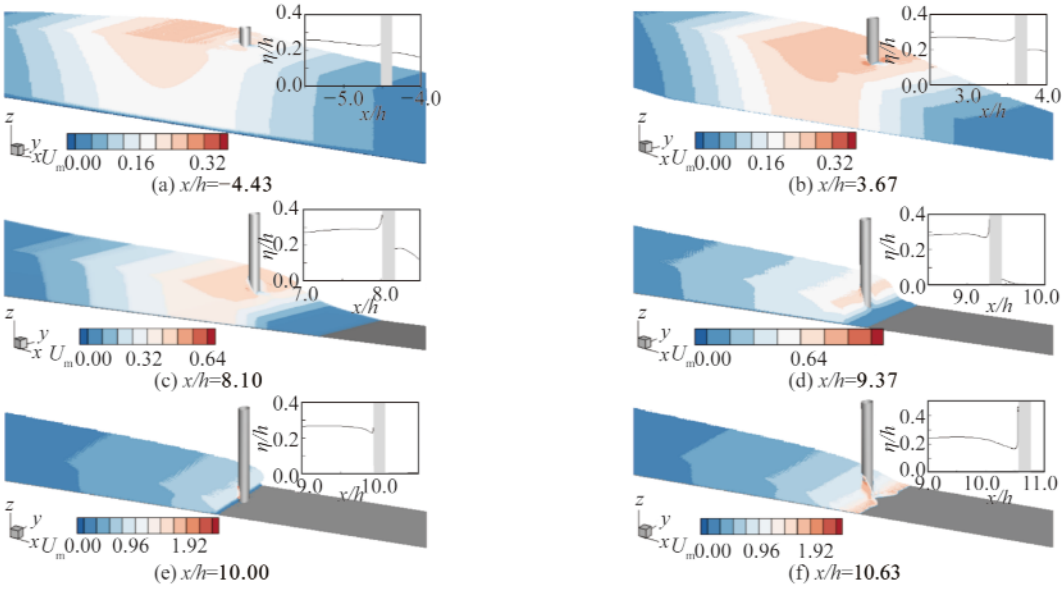

Fig. 18. Velocity fields and wave surface elevations around the cylinder at different locations (H/h = 0.274).

shown in Figs. 18d−18f.

The maximum wave force and fluid velocity values corresponding to different cylinder locations are shown in Fig. 19 alongside the maximum wave surface elevation in the front of the cylinder. The fluid velocity at different locations initially increases and then decreases, and the fluid velocity reaches the maximum when the cylinder is located at x/h = 9.84. The wave force exerted on the cylinder shows a similar changing trend with fluid velocity. Moreover, the wave force and fluid velocity reach their maxima when the cylinder is located at the same location. The variation of the maximum wave surface elevation in the front of the cylinder at different locations is complex because the wave breaks at x/h = 8.71.

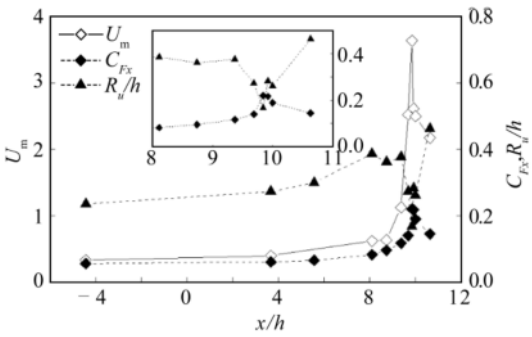

Fig. 19. Maximum fluid velocity, wave surface elevation in the front of the cylinder, and wave force for different cylinder locations (H/h = 0.274).

4.2.2 *Pressure around the cylinder at different locations*

Fig. 20 shows the distribution of relative pressure around the cylinder above the still-water level (i.e., z = 0) when C_{Fx} arrives at the maximum for the conditions of x/h = −4.43 to 9.84 and H/h = 0.274. The largest relative pressure is located in the front of the cylinder (α = 0°). The relative pressure begins to decrease from the front of the cylinder towards both sides and lower pressure is detected in the rear of the cylinder (α = −180° and +180°) owing to the cylinder's shielding effect. When the cylinder is located at x/h = −4.43 to 3.67, the water depth is relatively large, which leads to obscure deformation of the solitary wave. As a result, a smaller pressure difference is observed between α = 0° and 180°. Smaller wave forces are therefore exerted on cylinders at these locations.

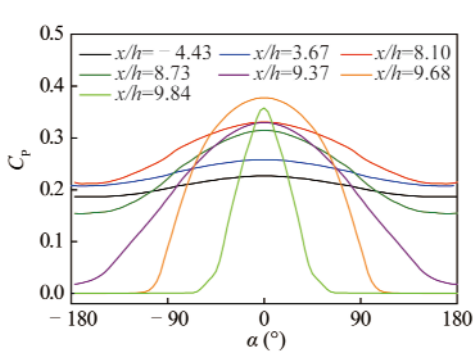

Fig. 20. Distribution of relative pressure on the cylinder when C_{Fx} arrives the maximum.

When the cylinder moves onshore, e.g., x/h = 8.10, the local still-water depth around the cylinder decreases. The deformation of solitary waves owing to shoaling leads to an increase of wave surface elevation. Consequently, the pressure in the front of the cylinder significantly increases, which leads to an increase of the pressure difference between α = 0° and 180°. As the cylinder further moves onshore, the local still-water depth around the cylinder decreases. The wave front becomes steeper and eventually the wave breaks, which leads to a decrease of wave surface elevation and an increase of fluid velocity. For these conditions, the maximum wave force appears before the wave wraps in the rear of the cylinder. Thus, the pressure in the rear of the cylinder decreases significantly, which leads to an increase of the pressure difference between α = 0° and 180°, e.g., x/h = 8.73−9.84.

The maximum wave force appears when the cylinder is located at x/h = 9.84. The pressure difference between the front and rear of the cylinder is smaller compared with that at x/h = 9.68, as shown in Fig. 20. This can be attributed to that when the wave force reaches the maximum, no wrap occurs on the cylinder in the domain of α= −180° to −90° and 90° to +180° for x/h=9.84, causing the pressure on the cylinder for α = −180° to −90° and 90° to +180° equal to zero in this case. However, part wrap can be observed on the cylinder in the domain of α= −180° to −90°and 90° to +180° for x/h=9.68. The relative pressure on the cylinder for α = −180° to −90° and 90° to +180° ranges from 0 to 0.1 for x/h = 9.68, which counterbalances some pressure from the front of the cylinder (α = –90° to 90°). As a result, the largest wave force on the cylinder appears at x/h = 9.84 in this study.

5 Conclusions

Wave forces on a cylinder located on a slope beach are numerically investigated using the Reynolds-averaged Navier–Stokes equations and standard k−ε turbulence model. The model is validated by comparing the numerical results with the existing experimental data. The wave forces and wave characteristics around the cylinder are studied. The effects of the relative incident wave height, KC number and cylinder location on the wave forces are analyzed and discussed. The following conclusions are drawn.

(1) Cylinder location strongly influences the maximum wave force exerted on the cylinder. When the cylinder is located in the water at a shallow local still-water depth, the wave forces acting on the cylinder can increase dramatically over a short time period owing to wave deformation and breaking, which shows that wave forces are evidently dependent on the cylinder location on the beach.

(2) The wave force exerted on the vertical cylinder increases power-exponentially with incident wave height and KC number. The wave force growth rate increases as the cylinder moves onshore, but when the location of the cylinder is above the still-water shoreline, its growth rate decreases.

(3) The wave force on the cylinder tends to initially increase and then decrease when the cylinder moves onshore. The maximum wave force appears when the cylinder is located at one cylinder diameter below the still-water shoreline.

(4) The fluid velocity initially increases slowly before x/h=8.00 and rapidly reach its maximum at x/h=9.84 and then decreases when the cylinder moves onshore. The fluid velocity arrives at its maximum with the maximal value of the wave force appearing at the same location. These maximum values appear prior to the wave surface elevation reaching its maximum in the front of the cylinder.

References

Adityawan, M.B., Tanaka, H. and Lin, P.Z., 2013. Boundary layer approach in the modeling of breaking solitary wave runup, *Coastal Engineering*, 73, 167–177.

Alagan Chella, M., Bihs, H., Myrhaug, D. and Muskulus, M., 2015. Breaking characteristics and geometric properties of spilling breakers over slopes, *Coastal Engineering*, 95, 4–19.

Alagan Chella, M., Bihs, H., Myrhaug, D. and Muskulus, M., 2017. Breaking solitary waves and breaking wave forces on a vertically mounted slender cylinder over an impermeable sloping seabed, *Journal of Ocean Engineering and Marine Energy*, 3, 1–19.

Alagan Chella, M., Tørum, A. and Myrhaug, D., 2012. An overview of wave impact forces on offshore wind turbine substructures, *Energy Procedia*, 20, 217–226.

Alsina, J.M., Falchetti, S. and Baldock, T.E., 2009. Measurements and modelling of the advection of suspended sediment in the swash zone by solitary waves, *Coastal Engineering*, 56(5–6), 621–631.

Aristodemo, F., Tripepi, G., Meringolo, D.D. and Veltri, P., 2017. Solitary wave-induced forces on horizontal circular cylinders: Laboratory experiments and SPH simulations, *Coastal Engineering*, 129, 17–35.

Aristodemo, F., Tripepi, G., Ferraro, D.A. and Veltri, P., 2020. An experimental and numerical study on solitary wave loads at cylinders near the bed, *Ocean Engineering*, 195, 106747.

Barth, T.J., 1992. *Aspects of Unstructured Grids and Finite-volume Solvers for the Euler and Navier−Stokes Equations*, AGARD, Paris.

Bonakdar, L., Oumeraci, H. and Etemad-Shahidi, A., 2015. Wave load formulae for prediction of wave-induced forces on a slender pile within pile groups, *Coastal Engineering*, 102, 49–68.

Boussinesq, J., 1872. Théorie des ondes et des remous qui se propagent le long d'un canal rectangulaire horizontal, en communiquant au liquide contenu dans ce canal des vitesses pareilles de la surface au fond, *Journal de Mathématiques Pures et Appliquées*, 2, 55–108. (in French)

Bredmose, H. and Jacobsen, N.G., 2010. Breaking wave impacts on offshore wind turbine foundations: Focused wave groups and CFD, *Proceedings of the ASME 2010 29th International Conference on Ocean*, *Offshore and Arctic Engineering*, ASME, Shanghai, China.

Chang, Y.H., Hwang, K.S. and Hwung, H.H., 2009. Large-scale laboratory measurements of solitary wave inundation on a 1:20 slope, *Coastal Engineering*, 56(10), 1022–1034.

Choi, S.J., Lee, K.H. and Gudmestad, O.T., 2015. The effect of dynamic amplification due to a structure's vibration on breaking wave impact, *Ocean Engineering*, 96, 8–20.

FEMA, 2004. *Final Draft Guidelines for Coastal Flood Hazard Analysis and Mapping for the Pacific Coast of the United States*, Northwest Hydraulic Consultants, Washington, D. C.

Goda, Y., Haranaka, S. and Kitahata, M., 1966. Study on impulsive breaking wave forces on piles, *Report Port and Harbour Technical Research Institute*, 6(5), 1–30.

Goring, D.G., 1978. *Tsunamis: the Propagation of Long Waves Onto A Shelf*, Rep.No.KH-R-38, California Institute of Technology, W.M. Keck Laboratory of Hydraulics and Water Resources, Pasadena, Calif.

Grilli, S.T., Svendsen, I.A. and Subramanya, R., 1997. Breaking criterion and characteristics for solitary waves on slopes, *Journal of Waterway*, *Port*, *Coastal*, *and Ocean Engineering*, 123(3), 102–112.

Hirt, C.W. and Nichols, D.B., 1981. Volume of fluid (VOF) method for the dynamics of free boundaries, *Journal of Computational Physics*, 39(1), 201–225.

Hsiao, S.C., Hsu, T.W., Lin, T.C. and Chang, Y.H., 2008. On the evolution and run-up of breaking solitary waves on a mild sloping beach, *Coastal Engineering*, 55(12), 975–988.

Hsieh, C.M., Cheng, M.H., Hwang, R.R. and Hsu, J.R.C., 2016. Numerical study on evolution of an internal solitary wave across an idealized shelf with different front slopes, *Applied Ocean Research*, 59, 236–253.

Issa, R.I., 1986. Solution of the implicitly discretised fluid flow equations by operator-splitting, *Journal of Computational Physics*, 62(1), 40–65.

Kamath, A., Chella, M.A., Bihs, H. and Arntsen, Ø.A., 2015. CFD investigations of wave interaction with a pair of large tandem cylinders, *Ocean Engineering*, 108, 738–748.

Kamath, A., Chella, M.A., Bihs, H. and Arntsen, Ø.A., 2016. Breaking wave interaction with a vertical cylinder and the effect of breaker location, *Ocean Engineering*, 128, 105–115.

Katell, G. and Eric, B., 2002. Accuracy of solitary wave generation by a piston wave maker, *Journal of Hydraulic Research*, 40(3), 321–331.

Kuai, Y.R., Qi, M.L. and Li, J.Z., 2018a. Numerical study on the propagation of solitary waves in the near-shore, *Ocean Engineering*, 165, 155–163.

Kuai, Y.R., Qi, M.L. and Li, J.Z., 2018b. Analysis of wave forces on bridge substructure in near-shore, *Journal of Zhejiang University* (*Engineering Science*), 52(12), 2356–3264. (in Chinese)

Launder, B.E. and Spalding, D.B., 1974. The numerical computation of turbulent flows, *Computer Methods in Applied Mechanics and Engineering*, 3(2), 269–289.

Madsen, P.A., Fuhrman, D.R. and Schäffer, H.A., 2008. On the solitary wave paradigm for tsunamis, *Journal of Geophysical Research*: *Oceans*, 113(C12), C12012.

Mo, W., Irschik, K., Oumeraci, H. and Liu, P.L.F., 2007. A 3D numerical model for computing non-breaking wave forces on slender piles, *Journal of Engineering Mathematics*, 58(1–4), 19–30.

Mo, W.H., Jensen, A. and Liu, P.L.F., 2013. Plunging solitary wave and its interaction with a slender cylinder on a sloping beach, *Ocean Engineering*, 74, 48–60.

Mori, N., Takahashi, T., Yasuda, T. and Yanagisawa, H., 2011. Survey of 2011 Tohoku earthquake tsunami inundation and run-up, *Geophysical Research Letters*, 38(7), L00G14.

Morison, J.R., Johnson, J.W. and Schaaf, S.A., 1950. The force exerted by surface waves on piles, *Journal of Petroleum Technology*, 2(5), 149–154.

Rayleigh, L., 1876. XXXII. On waves, *The London*, *Edinburgh*, *and Dublin Philosophical Magazine and Journal of Science*, 1(4), 257–279.

Sælevik, G., Jensen, A. and Pedersen, G., 2013. Runup of solitary waves on a straight and a composite beach, *Coastal Engineering*, 77, 40–48.

Sumer, B.M., Sen, M.B., Karagali, I., Ceren, B., Fredsøe, J., Sottile, M., Zilioli, L. and Fuhrman, D.R., 2011. Flow and sediment transport induced by a plunging solitary wave, *Journal of Geophysical Research*: *Oceans*, 116(C1), C01008.

Synolakis, C.E., 1987. The runup of solitary waves, *Journal of Fluid Mechanics*, 185, 523–545.

Tripepi, G., Aristodemo, F. and Veltri, P., 2018. On-bottom stability analysis of cylinders under tsunami-like solitary waves, *Water*, 10(4), 487.

Wienke, J. and Oumeraci, H., 2005. Breaking wave impact force on a vertical and inclined slender pile-theoretical and large-scale model investigations, *Coastal Engineering*, 52(5), 435–462.

Xiao, H. and Huang, W.R., 2015. Three-dimensional numerical modeling of solitary wave breaking and force on a cylinder pile in a coastal surf zone, *Journal of Engineering Mechanics*, 141(8), A4014001.

Yang, C., Liu, Y. and Liu, C.G., 2015. Predicting wave loads on adjacent cylinder arrays with a 3D model, *Journal of Hydraulic Research*, 53(6), 797–807.

Yates, G.T. and Wang, K.H., 1994. Solitary wave scattering by a vertical cylinder: experimental study, *Proceedings of the 4th International Offshore and Polar Engineering Conference*, ISOPE, Osaka, pp. 118–124.

Youngs, D.L., 1982. Time-dependent multi-material flow with large fluid distortion, in: Morton, K.W. and Baines, M.J. (eds.), *Numerical Methods for Fluid Dynamics*, Academic Press, New York.

Zhao, M., Cheng, L. and Teng, B., 2007. Numerical simulation of solitary wave scattering by a circular cylinder array, *Ocean Engineering*, 34(3–4), 489–499.

Zhao, X.Z., Cheng, D., Zhang, Y.F. and Li, M.Y., 2019. Experimental and numerical study on the hydrodynamic characteristics of solitary waves passing over a submerged breakwater, *China Ocean Engineering*, 33(3), 253–267.